JOURNAL OF APPLIED CRYSTALLOGRAPHY
ISSN 1600-5767

Structure evolution of Bi_4O_7 under high pressure

Jianzong Wang,[a] Luhong Wang,[b]* Fuyang Liu,[a] Shuhua Yuan,[a] Dongzhou Zhang,[c,d] Vitali B. Prakapenka,[d] Wilhelm Klein[e] and Haozhe Liu[a]*

[a]Center for High Pressure Science and Technology Advanced Research, Beijing 10094, People's Republic of China, [b]Shanghai Advanced Research in Physical Sciences, Shanghai 201203, People's Republic of China, [c]PX2, Hawaii Institute of Geophysics and Planetology, University of Hawaii at Manoa, Honolulu, Hawaii 96822, USA, [d]Center for Advanced Radiation Sources, University of Chicago, Chicago, Illinois 60439, USA, and [e]Department of Chemistry, School of Natural Sciences, Technical University of Munich, 85748 Garching, Germany. *Correspondence e-mail: luhongwang@hotmail.com, haozhe.liu@hpstar.ac.cn

Received 15 May 2023
Accepted 8 June 2023

Edited by S. Moggach, The University of Western Australia, Australia

Keywords: high pressure; structure; X-ray diffraction; XRD; compressibility; bismuth oxide.

Supporting information: this article has supporting information at journals.iucr.org/j

X-ray diffraction and Raman spectroscopy measurements were used to study the structure evolution of Bi_4O_7 during compression. Two isostructural phase transitions were observed under high pressure, with the first transition to phase II occurring at approximately 3.0 (2) GPa and the second to phase III occurring at approximately 13.0 (5) GPa. The pressure–volume (P–V) curve was found to be discontinuous at those two pressure transition boundaries. By fitting the P–V curves in three different stages, the bulk moduli were estimated to be approximately 101 (2), 68 (2) and 172 (3) GPa. Such large differences in the bulk moduli confirm two isostructural phase changes in the three stages. An irreversible amorphization process was found to start at approximately 20 (1) GPa, and the sample gradually becomes fully amorphous during compression at 30 (1) GPa.

1. Introduction

Recently, bismuth and antimony oxides have attracted much attention in fundamental research due to the nonbonding lone electron pairs in their 6*s* and 5*s* orbitals (Carey *et al.*, 2014; Egorysheva *et al.*, 2020; Pereira *et al.*, 2013), while the unique structures of these oxides show potential for a rich array of applications, especially in photosensitive semiconductors (Hameed *et al.*, 2008; Zhang *et al.*, 2018; Pérez-Mezcua *et al.*, 2016; Fujita *et al.*, 2020; Jia *et al.*, 2020; Sun *et al.*, 2017). For instance, as a new ceramic semiconductor, Bi_3SbO_7 is a low-temperature co-fired ceramic with high-quality application prospects (Pang *et al.*, 2011). Additionally, bismuth oxide exhibits excellent performance in the field of catalysis and Bi_2O_3 plays an important role in conversion treatments of NO waste gas (Cabot *et al.*, 2004). α-Bi_2O_3 undergoes amorphization induced by high pressure (Pereira *et al.*, 2013; Chouinard & Desgreniers, 1999), and the isostructural phase transition of β-Bi_2O_3 occurs at 2 GPa (Pereira *et al.*, 2014). The cubic phase δ-Bi_2O_3, the tetragonal phase ε-Bi_2O_3 and the high-pressure hexagonal phase HP-Bi_2O_3 have been studied, and interesting high-pressure structures have been found (Yashima & Ishimura, 2003; Cornei *et al.*, 2006; Locherer *et al.*, 2011; Ghedia *et al.*, 2010). At present, abnormal compressibility has not been observed for bismuth oxide during its phase transitions. In this study, the rare phenomenon of a relatively soft stage in Bi_4O_7 was observed via *in situ* Raman spectroscopy and synchrotron X-ray diffraction (XRD) under high pressure, which resembled the phase becoming mechanically softer during compression in other systems, such

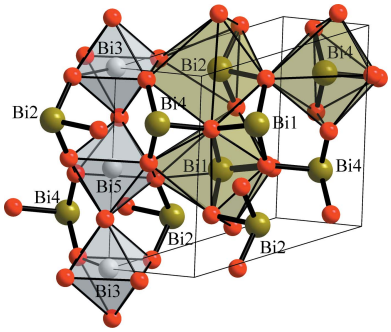

as metal–organic frameworks (Cairns *et al.*, 2013; Goodwin *et al.*, 2008; Chapman & Chupas, 2007).

Bismuth is a Group 15 metal, and the oxide contains Bi^{3+} and Bi^{5+} in a mixed-valent triclinic crystalline phase of Bi_4O_7 (Begemann & Jansen, 1989). The high-pressure structural evolution of Bi_4O_7 has not been reported previously. In this article, Bi_4O_7 was studied using the characterization of the shift of Raman modes related to crystal compressibility under high pressure, similar to the method used previously (Efthimiopoulos *et al.*, 2014). It was found that the structure has an abnormal compressibility enhancement trend during compression, which is contrary to the decreasing trend of compressibility of other binary Bi–O compounds, such as Bi_2O_3, under high pressure (Pereira *et al.*, 2014; Locherer *et al.*, 2011). As shown in previous studies of the abnormal compressibilities in zeolites (Gatta & Lee, 2014), the increase in the compressibility of Bi_4O_7 might be caused by the entry of silicone oil into the structure. Therefore, two separate experimental runs with and without pressure medium were performed. In addition, synchrotron XRD experiments on Bi_4O_7 were carried out to analyze the change of the bulk modulus under high pressure, and an abnormal softening in the bulk modulus was found.

2. Experimental methods

2.1. Synthesis

$NaBiO_3$ (10 g; Merck, p.a.) was reacted in each case in an ice/salt bath with concentrated HNO_3 (100 ml) cooled to 273 K, suctioned off after 10 min and washed with cold water. The product was dried in a desiccator over phosphorus pentoxide for a period of one week. The resulting X-ray-amorphous brown powder was placed in a gold tube, which was sealed on one side and mechanically closed (not gas-tight) on the other, and finally placed in a stainless steel autoclave (Linke & Jansen, 1997), where water (1 ml) was added as a mineralizer. Pure samples of Bi_4O_7 were obtained under elevated oxygen pressures of 400 MPa at 300 °C.

2.2. XRD experiment

In situ high-pressure XRD measurements were conducted on a powdered sample of Bi_4O_7 that was compressed up to 30 GPa at room temperature, with a wavelength of 0.4340 Å from beamline 13-BM-C at APS, Argonne National Laboratory. The powdered sample was loaded into a diamond anvil cell (DAC) chamber with a culet size of 300 µm. T301 stainless steel was used as the gasket. Au was used as the pressure marker (Takemura & Dewaele, 2008) and silicone oil (Shen *et al.*, 2004) was used as the pressure-transmitting medium.

2.3. Raman spectroscopy experiment

In the Raman measurements, a DAC with 500 µm culets was used, and T301 stainless steel was used as the gasket without a pressure-transmitting medium. A separate experiment was conducted using silicone oil as the pressure-transmitting medium. The pressure was calibrated using the ruby fluorescence method (Shen *et al.*, 2021). The Raman instrument was a MonoVista CRS+ confocal Raman spectrometer from Spectroscopy & Imaging GmbH. The spectrometer had a resolution of 0.2 cm^{-1} FWHM at a laser wavelength of 633 nm, and a

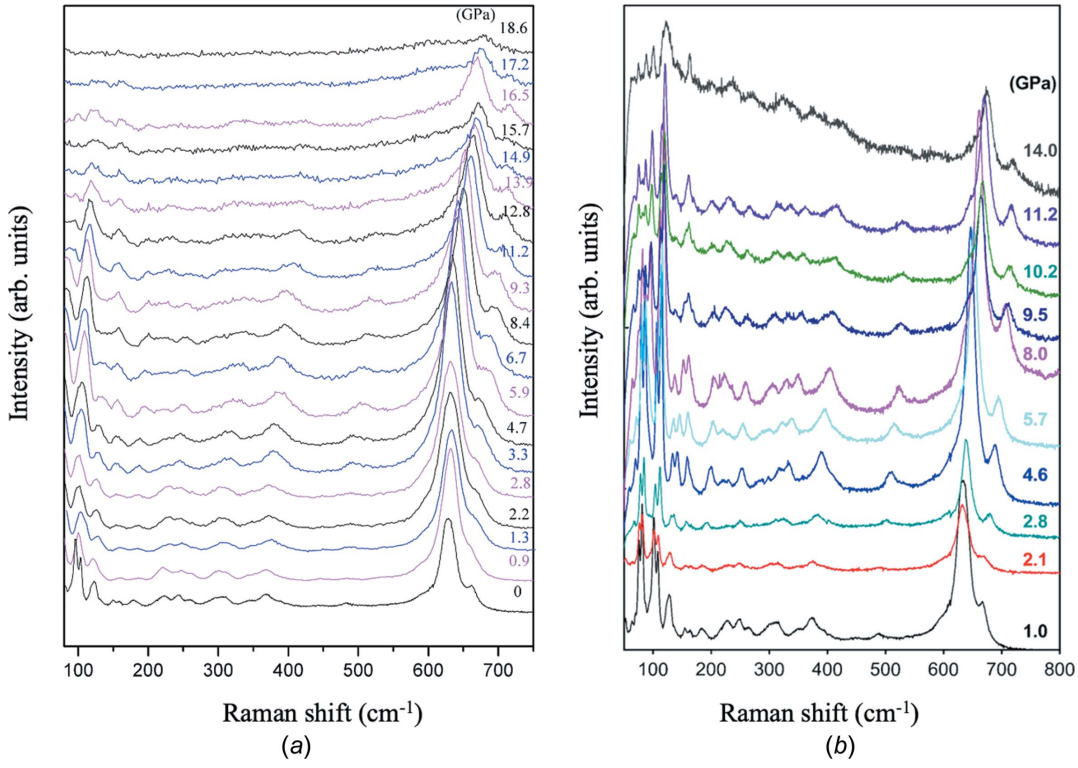

Figure 1
Raman spectra of Bi_4O_7 during compression (*a*) without a pressure-transmitting medium and (*b*) with silicone oil as the pressure-transmitting medium.

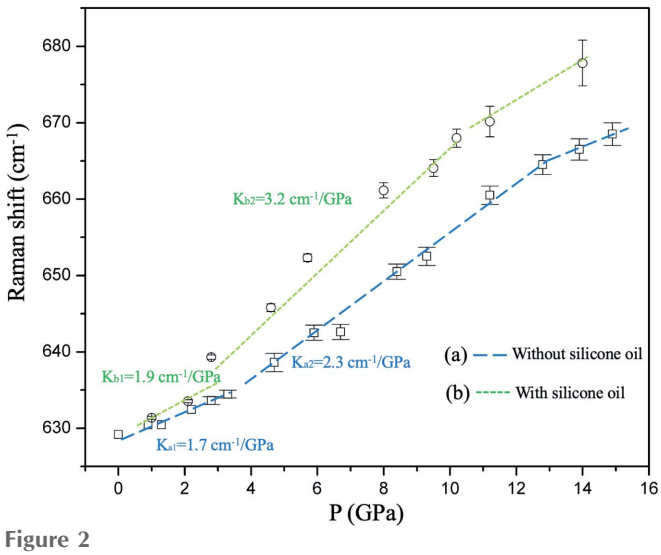

Figure 2
The shifts of the strongest Raman peak of Bi_4O_7 during compression. The blue dashed line represents the results without a pressure-transmitting medium and the green dashed line represents the results with the pressure-transmitting medium. Some error bars were smaller than the size of the data symbols, and the typical pressure error bars were around 0.1–0.2 GPa.

power of 1.820 mW was used. The exposure time was 1 s and the spectrum was averaged over 300 measurements at room temperature.

3. Results and discussion

Raman spectroscopy is a sensitive tool for detecting local structure change during phase transitions. As shown in Fig. 1, the Raman spectra of Bi_4O_7, which includes 30 A_g active modes according to group theory, showed variations under high pressure and are in good agreement with a previous report (Depablos-Rivera *et al.*, 2021). During compression, all the Raman-active modes moved from low frequency to higher frequency. The evolution of the strongest Raman mode was selected as the typical characterization of crystal compressibility.

In the previous report (Depablos-Rivera *et al.*, 2021), the density functional approximation was used to calculate the Raman-active modes in Bi_4O_7. The intense mode at around 629 cm^{-1} was proposed to be related to the stretching vibration modes in a component of [BiO_n] polyhedra, such as BiO_3 and BiO_4. Here, this Raman mode was used as an indicator for the compressibility change upon compression. Fig. 2 shows the trend of this shift in Raman mode under high pressure. When the pressure was above 3 GPa, the vibration peak near 629 cm^{-1} showed an abnormally large Raman shift according to the two independent Raman experiments, which may be related to the formation of a new phase (Efthimiopoulos *et al.*, 2014). In the absence of a pressure-transmitting medium, the compressibility of crystals will decrease slightly in nonhydrostatic environments, and the blue dashed line shifted more slowly than the green dashed line. There was indeed a slight acceleration of shift of the Raman peaks when the pressure medium was used. However, the results of both Raman experiments indicated an abnormal shift acceleration under high pressure in the range 3–12 GPa. The compressibility of Bi_4O_7 may increase abnormally during this compression range. In addition, due to the potential amorphization of Bi_4O_7 at a pressure over 17 GPa, the Raman-active modes gradually vanished.

In the XRD experiment, a silicone oil pressure medium was used and the pressure reached 30.8 GPa at room temperature.

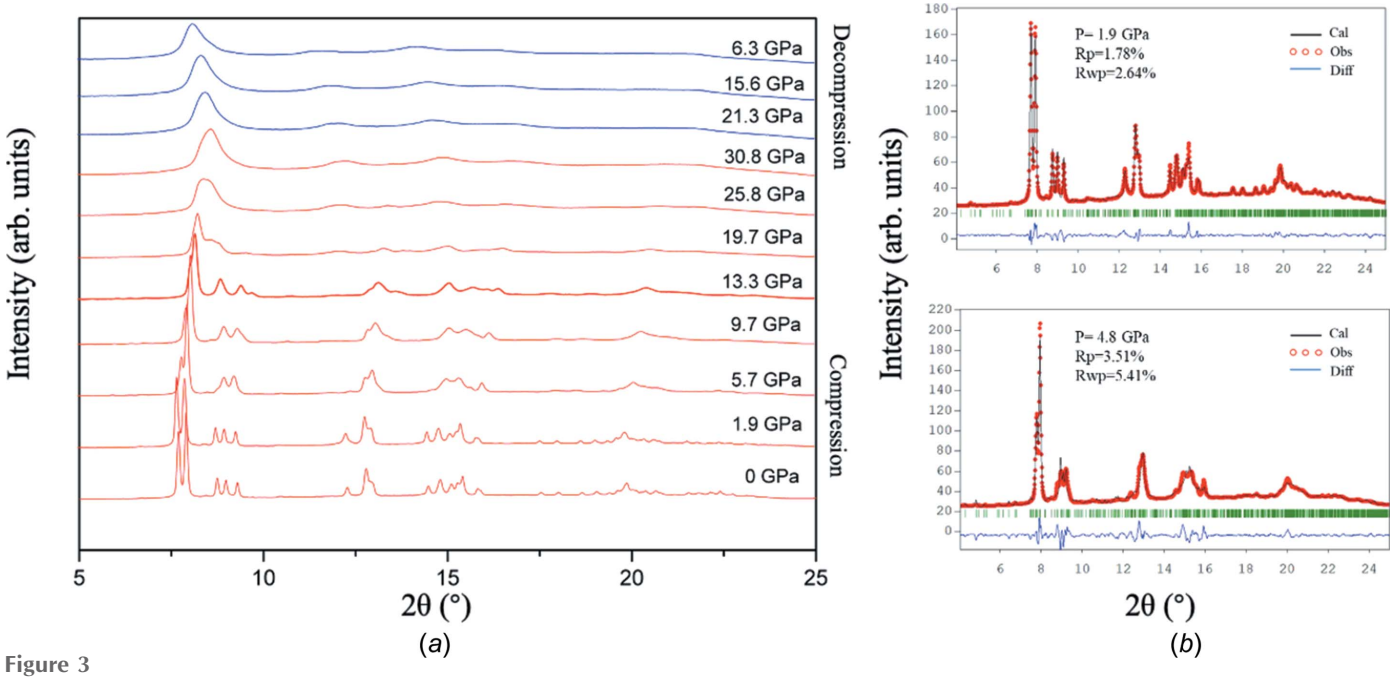

Figure 3
(*a*) Selected XRD patterns for Bi_4O_7 recorded during the compression and decompression process at room temperature. (*b*) Two selected typical refinement results for the XRD pattern of Bi_4O_7 obtained at 1.9 and 4.8 GPa.

The typical XRD patterns at various pressures are shown in Fig. 3(*a*). The diffraction peaks of Bi_4O_7 showed a transition to an amorphous state, which was consistent with the Raman results obtained above 17 GPa. The XRD pattern obtained during the decompression process indicates that an irreversible amorphization of the crystal occurred upon compression.

The compressibility of Bi_4O_7 undergoes abnormal changes according to the shift of the Raman modes under high pressure. The abnormal compressibility of the crystals was further verified by contrasting the compressibility of the crystal volume under high pressure. The *POWDER CELL* and *GSAS* programs were used to perform Le Bail refinement (Kraus & Nolze, 1996; Toby, 2001), and two selected typical XRD refinement results were shown in Fig. 3(*b*). The *P*–*V* curve was fitted with the second-order Birch–Murnaghan equation of state (EOS) to calculate the bulk modulus (Vinet *et al.*, 1986), in which the B_0 is the bulk modulus while B_0' is fixed at 4 (Occelli *et al.*, 2004; Li *et al.*, 2020).

As shown in Fig. 4, consistent with the trend in the changes of the Raman mode, the *P*–*V* data were divided into four stages, *i.e.* 0–3, 3–12 and 12–21 GPa and the amorphous state at pressures above 21 GPa. Two isostructural transitions were observed, a situation similar to the pressure-induced isostructural transitions in the $Bi_{14}CrO_{24}$ system (Errandonea *et al.*, 2014). The first stage is considered as phase I. In this region, the bulk modulus was estimated as 101 (2) GPa. The bulk modulus of the second stage, which is labelled as phase II, decreased by more than 30% to 68 (2) GPa, an unusual increase in the compressibility, which is consistent with the compressibility enhancement represented by the Raman mode shift. The bulk modulus is quite close to the bulk moduli of the ambient phase and the isostructural high-pressure phase in the $Bi_{14}CrO_{24}$ system (Errandonea *et al.*, 2014). The pressure-driven rearrangement of the BiO_{3+4} trigonal pyramids caused the relatively soft stage with greater compressibility in phase II. Similar, but not so common, abnormal compressibilities were also seen for ReO_3 and δ-UO_3, which were related to structural distortion upon compression (Dyuzheva *et al.*, 2001; Schirber *et al.*, 1979). As the pressure was increased above 13 GPa to reach the third stage, the bulk modulus of phase III increased to 172 (3) GPa, which was partially caused by the increase in Coulombic repulsion due to the effect of pressure on the stereochemical activity of the Bi^{3+} lone electron pair in the BiO_{3+4} clusters (Bu *et al.*, 2020; Gribchenkova *et al.*, 2007).

Structural information concerning bismuth oxides is usually difficult to obtain owing to the different scattering powers of the two elements, and the crystal structure of Bi_4O_7 was determined previously from high-resolution X-ray and neutron powder data (Dinnebier *et al.*, 2002). The parameters of this structure determination were used for our structure considerations also at high pressures, as reliable Rietveld refinements were not possible on the high-pressure powder X-ray diffraction data. The structure crystallizes in the triclinic space group $P\bar{1}$ and exhibits five crystallographic positions for Bi atoms, which can be clearly assigned to the different oxidation states +III and +V according to their O-atom coordination. Two different sites for Bi^{5+} at special Wyckoff positions 1*a* and 1*b* are coordinated by slightly distorted octahedra of O atoms, which form corner-sharing strands along the crystallographic *c* axis (Fig. 5). Three independent Bi^{3+} atoms at general 2*i* positions have three neighbouring O atoms each, forming trigonal pyramids which connect the above-mentioned strands of octahedra *via* common vertices. Regarding the oxygen environment in all directions, the three different Bi^{3+} atoms are surrounded by irregular polyhedra with three shorter and either four of five longer Bi—O distances, thus showing a distinct lone-pair effect for all the

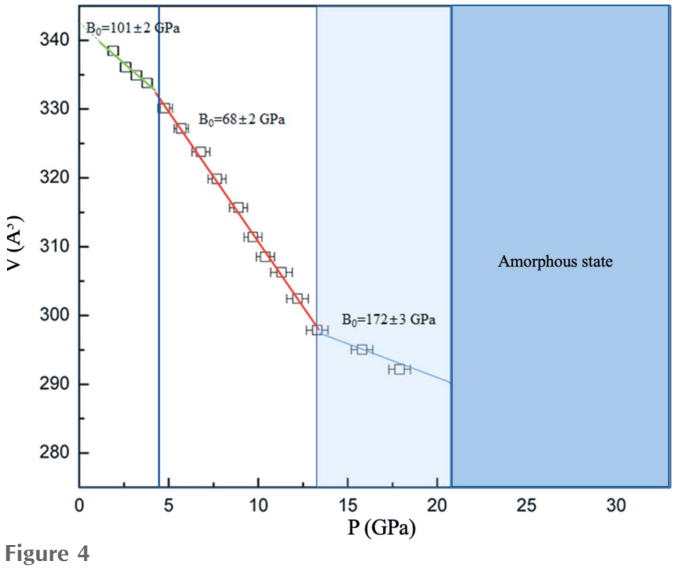

Figure 4
The volume (*V*) and pressure (*P*) relationship for Bi_4O_7. The green, red and blue solid lines are the fitted results according to isothermal EOSs. The error bars for volume were smaller than the size of the data symbols, and the typical pressure error bars were around 0.2–1.0 GPa.

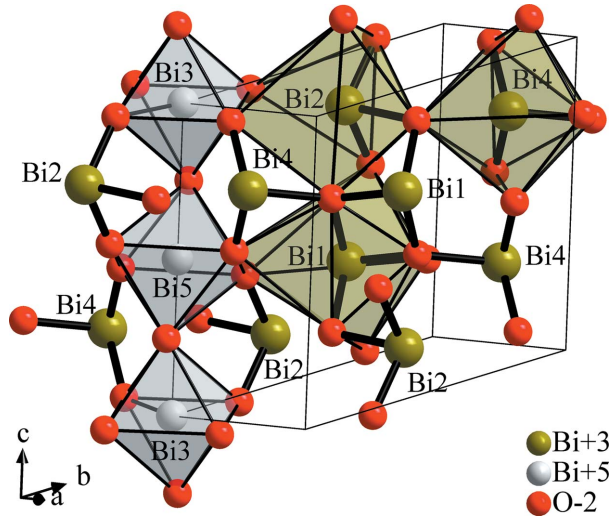

Figure 5
Section of the crystal structure of Bi_4O_7 under ambient conditions, emphasizing the different oxidation states of Bi. Shown are one strand of $Bi^{5+}O_6$ octahedra and neighbouring $Bi^{3+}O_3$ groups, and for each independent Bi^{3+} atom, one surrounding irregular oxygen polyhedron is drawn.

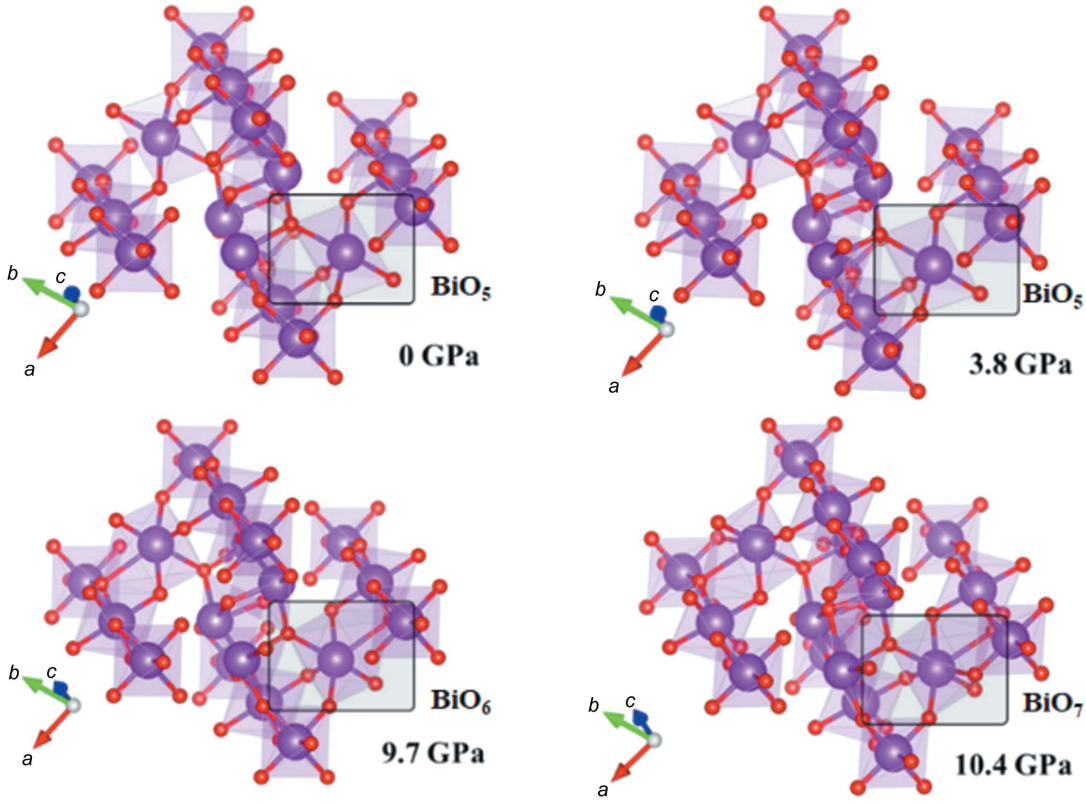

Figure 6
The crystal structure evolution of Bi_4O_7 from an open-framework structure to a compact structure upon compression.

Bi^{3+} sites. The structure can be regarded as a distorted defect variant of the fluorite structure type (Dinnebier *et al.*, 2002).

The application of pressure to the structure results in a volume decrease mainly shown in the crystallographic *a* and *b* axes, while the *c* axis shrinks to a smaller degree (see Table S1 in the supporting information). This indicates the higher stability of the $Bi^{5+}O_6$ octahedra, which are arranged along the *c* axis. Similar findings were observed in $BiSbO_4$, where the $Sb^{5+}O_6$ octahedra are much more stable against compression than the $Bi^{3+}O_{3+4}$ polyhedra (Errandonea *et al.*, 2016).

The compressibility of the orthogonal axes (the principal axes) was analyzed briefly using *PASCal* (Cliffe & Goodwin, 2012). The corresponding principal compressibilities were estimated as 3.05, 3.68 and 1.42 TPa^{-1} at a pressure of 10.4 GPa, indicating a strong anisotropic compression feature. Generally, the decrease in the Bi—O distances is more or less insignificant and no clear trend for a difference between the Bi^{5+}—O and Bi^{3+}—O contacts, irrespective of bonding or nonbonding, is observable, as illustrated by the relative decrease listed in Tables S2–S6 (see supporting information).

However, the absolute values of some of the nonbonding Bi—O distances occur in a range which might be considered as bonding, so if a bond length of 2.67 Å was set as the threshold bond length for coordination, then, for example, the pseudo-coordination number of the Bi4 atom increases from 5 to 7 upon compression from phase I to phase II, as shown in Fig. 6. The abnormal compressibility change occurred in this sample from an open-framework-type structure under ambient conditions to a relatively soft stage of pressure-driven rearrangement of the BiO_{3+4} trigonal pyramids, and then to a relatively compact structure in the higher-pressure region above 13 GPa. The difference in strengths for the Bi–O polyhedra decreased at higher pressure, and then it was difficult to have abnormal compression enhancement above 13 GPa. Phase III showed that Bi_4O_7 had lower compressibility due to the enhanced Coulombic force, which eventually destroyed the crystalline structure, and the sample entered into an amorphous state after phase III. Potential charge transfer might happen under high-pressure conditions, and high-resolution diffraction data combined with other *in situ* characterization techniques will be required to answer this question.

4. Conclusions

In this study, X-ray diffraction and Raman spectroscopy techniques were used to investigate the structural evolution of Bi_4O_7 under high pressure up to 30 GPa. Two isostructural transitions were found at 3 and 13 GPa, which correspond to an abnormal compressibility change, and the crystalline structure transformed from an open-framework type to a more compact structure. Further compression resulted in the sample undergoing irreversible amorphization beyond 20 GPa.

Funding information

This work was supported by the Natural Science Foundation of China (11374075). Portions of this work were performed at

GeoSoilEnviroCARS (The University of Chicago), Advanced Photon Source (APS), Argonne National Laboratory. GeoSoilEnviroCARS is supported by the National Science Foundation–Earth Sciences (EAR-1634415) and the US Department of Energy–GeoSciences (DE-FG02-94ER14466). This research used resources of the Advanced Photon Source, a US Department of Energy (DOE) Office of Science User Facility operated for the DOE Office of Science by Argonne National Laboratory under contract No. DE-AC02-06CH11357).

References

Begemann, B. & Jansen, M. (1989). *J. Less-Common Met.* **156**, 123–135.
Bu, K., Luo, H., Guo, S., Li, M., Wang, D., Dong, H., Ding, Y., Yang, W. & Lü, X. (2020). *J. Phys. Chem. Lett.* **11**, 9702–9707.
Cabot, A., Marsal, A., Arbiol, J. & Morante, J. R. (2004). *Sens. Actuators B Chem.* **99**, 74–89.
Cairns, A. B., Catafesta, J., Levelut, C., Rouquette, J., van der Lee, A., Peters, L., Thompson, A. L., Dmitriev, V., Haines, J. & Goodwin, A. L. (2013). *Nat. Mater.* **12**, 212–216.
Carey, J. J., Allen, J. P., Scanlon, D. O. & Watson, G. W. (2014). *J. Solid State Chem.* **213**, 116–125.
Chapman, K. W. & Chupas, P. J. (2007). *J. Am. Chem. Soc.* **129**, 10090–10091.
Chouinard, C. & Desgreniers, S. (1999). *Solid State Commun.* **113**, 125–129.
Cliffe, M. J. & Goodwin, A. L. (2012). *J. Appl. Cryst.* **45**, 1321–1329.
Cornei, N. T. N., Tancret, N., Abraham, F. & Mentré, O. (2006). *Inorg. Chem.* **45**, 4886–4888.
Depablos-Rivera, O., Martínez, A. & Rodil, S. E. (2021). *J. Alloys Compd.* **853**, 157245.
Dinnebier, R. E., Ibberson, R. M., Ehrenberg, H. & Jansen, M. (2002). *J. Solid State Chem.* **163**, 332–339.
Dyuzheva, T. I., Bendeliani, N. A., Brazhkin, V. V. & Kuznetshov, L. M. (2001). *J. Alloys Compd.* **315**, 59–61.
Efthimiopoulos, I., Kemichick, J., Zhou, X., Khare, S. V., Ikuta, D. & Wang, Y. (2014). *J. Phys. Chem. A*, **118**, 1713–1720.
Egorysheva, A. V., Golodukhina, S. V., Khoroshilov, A. V., Tyurin, A. V., Gajtko, O. M., Svetogorov, R. D. & Trigub, A. L. (2020). *Ceram. Int.* **46**, 7413–7420.
Errandonea, D., Muñoz, A., Rodríguez-Hernández, P., Gomis, O., Achary, S. N., Popescu, C., Patwe, S. J. & Tyagi, A. K. (2016). *Inorg. Chem.* **55**, 4958–4969.
Errandonea, D., Santamaria-Perez, D., Achary, S. N. & Tyagi, A. K. (2014). *Solid State Commun.* **182**, 50–54.
Fujita, I., Edalati, P., Wang, Q., Watanabe, M., Arita, M., Munetoh, S., Ishihara, T. & Edalati, K. (2020). *Scr. Mater.* **187**, 366–370.
Gatta, G. D. & Lee, Y. (2014). *Miner. Mag.* **78**, 267–291.
Ghedia, S., Locherer, T., Dinnebier, R., Prasad, D. L. V. K., Wedig, U., Jansen, M. & Senyshyn, A. (2010). *Phys. Rev. B*, **82**, 024106.
Goodwin, A. L., Keen, D. A. & Tucker, M. G. (2008). *Proc. Natl Acad. Sci. USA*, **105**, 18708–18713.
Gribchenkova, N. A., Steblevskii, A. V., Kolosov, E. N., Alikhanian, A. S. & Nipan, G. D. (2007). *Inorg. Mater.* **43**, 78–84.
Hameed, A., Montini, T., Gombac, V. & Fornasiero, P. (2008). *J. Am. Chem. Soc.* **130**, 9658–9659.
Jia, Y., Li, S., Ma, H., Gao, J., Zhu, G., Zhang, F., Park, J. Y., Cha, S., Bae, J. S. & Liu, C. (2020). *J. Hazard. Mater.* **382**, 121121.
Kraus, W. & Nolze, G. (1996). *J. Appl. Cryst.* **29**, 301–303.
Li, Y., Ye, M., Tang, R., Chen, J., Qu, X., Yang, B., Wang, X., Yue, H. & Zhu, P. (2020). *Phys. Chem. Chem. Phys.* **22**, 13136–13142.
Linke, C. & Jansen, M. (1997). *Z. Anorg. Allg. Chem.* **623**, 1441–1446.
Locherer, T., Prasad, D. L. V. K., Dinnebier, R., Wedig, U., Jansen, M., Garbarino, G. & Hansen, T. (2011). *Phys. Rev. B*, **83**, 214102.
Occelli, F., Farber, D. L., Badro, J., Aracne, C. M., Teter, D. M., Hanfland, M., Canny, B. & Couzinet, B. (2004). *Phys. Rev. Lett.* **93**, 095502.
Pang, L. X., Zhou, D., Wang, H., Wu, Y., Guo, J. & Chen, Y. H. (2011). *J. Phys. Chem. Solids*, **72**, 882–885.
Pereira, A. L. J., Errandonea, D., Beltrán, A., Gracia, L., Gomis, O., Sans, J. A., García-Domene, B., Miquel-Veyrat, A., Manjón, F. J., Muñoz, A. & Popescu, C. (2013). *J. Phys. Condens. Matter*, **25**, 475402.
Pereira, A. L. J., Sans, J. A., Vilaplana, R., Gomis, O., Manjón, F. J., Rodríguez-Hernández, P., Muñoz, A., Popescu, C. & Beltrán, A. (2014). *J. Phys. Chem. C*, **118**, 23189–23201.
Pérez-Mezcua, D., Bretos, I., Jiménez, R., Ricote, J., Jiménez-Rioboó, R. J., da Silva, C. G., Chateigner, D., Fuentes-Cobas, L., Sirera, R. & Calzada, M. L. (2016). *Sci. Rep.* **6**, 39561.
Schirber, J. E., Azevedo, L. J. & Narath, A. (1979). *Phys. Rev. B*, **20**, 4746–4747.
Shen, G., Smith, J. S., Kenney-Benson, C. & Klotz, S. (2021). *High Pressure Res.* **41**, 175–183.
Shen, Y., Kumar, R. S., Pravica, M. & Nicol, M. F. (2004). *Rev. Sci. Instrum.* **75**, 4450–4454.
Sun, M., Wang, Y., Shao, Y., He, Y., Zeng, Q., Liang, H., Yan, T. & Du, B. (2017). *J. Colloid Interface Sci.* **501**, 123–132.
Takemura, K. & Dewaele, A. (2008). *Phys. Rev. B*, **78**, 104119.
Toby, B. H. (2001). *J. Appl. Cryst.* **34**, 210–213.
Vinet, P., Ferrante, J., Smith, J. R. & Rose, J. H. (1986). *J. Phys. C. Solid State Phys.* **19**, L467–L473.
Yashima, M. & Ishimura, D. (2003). *Chem. Phys. Lett.* **378**, 395–399.
Zhang, C., Li, X., Zheng, S., Ma, Y., Hu, C., Li, C., Duo, S. & Hu, Q. (2018). *Colloids Surf. A Physicochem. Eng. Asp.* **548**, 150–157.